10 Magnetic and Thermal Properties of Superconducting and Related Materials

H. Keller, C. Aegerter, J. Hofer, V.A. Ivanshin (visiting scientist), S. Romer (till Feb. 98), A. Schilling (since Oct. 97), A. Shengelaya, M. Willemin, G.M. Zhao, and K.A. Müller (Honorarprofessor)

10.1 Introduction

Over the past year we have continued and extended our investigations of the magnetic properties of high-temperature superconductors and related magnetic systems. In order to achieve this goal we have used a combination of muon spin rotation (μSR), neutron scattering, electron paramagnetic resonance (EPR), together with bulk SQUID and torque magnetometry measurements, and thermal expansion measurements.

In addition to our well established activities at the muon beams of PSI (Paul Scherrer Institute) and RAL (Rutherford Appleton Laboratory), we have over the past few years become increasingly involved in the investigation of vortex lattices using neutron scattering techniques. Up to now, these studies have been carried out at the ILL (Institut Laue Langevin), but with the advent of the neutron spallation source SINQ at PSI, we hope to carry out some of our future neutron work there (see Sec 10.2).

In order to complete our recent development of microscopic torquemeters (see also Annual Report 96/97), we designed a larger torque sensor for measuring with an optimized sensitivity millimeter size samples (see Sec 10.3.1).

During the last year torque magnetization measurements on $HgBa_2CuO_{4+\delta}$ single crystals with different oxygen doping δ were performed in order to reveal the doping dependence of the effective mass anisotropy $\gamma = \sqrt{m_c^*/m_{ab}^*}$, and of the in-plane penetration depth λ_{ab}. The observed monotonic increase of γ with decreasing δ is well described by a (bi)polaronic model of high-T_c superconductivity (see Sec. 10.3.2).

Electron Paramagnetic Resonance (EPR) is a powerful tool in solid state physics, which allows to study crystal electric fields, electron-phonon interactions, static and dynamic magnetic correlations on a *microscopic* level. EPR is a contactless method, thus the samples of any form (powder, pellet, single crystal, thin film) can be measured. Due to the extreme sensitivity of EPR, only a tiny amount of material is necessary. Our research interest during the last year was mainly concerned with hole-doped quasi-1D copper-oxygen chain systems (see Sec.10.4.1) and high-T_c cuprates (see Sec.10.4.2).

We have continued our studies of oxygen-isotope effects in the giant magnetoresistance manganites $La_{1-x}Me_xMnO_3$ (Me = Ca, Sr, and Ba) by means of magnetization and resistivity measurements, as well as measurements of the thermal expansion coefficient (see Annual Report 96/97). As a result of this study, we discovered a novel metal-insulator transion induced by oxygen isotope exchange in $(La_{0.5}Nd_{0.5})_{0.67}Ca_{0.33}MnO_3$ (see Sec. 10.5.1). Furthermore, we have completed our study of the oxygen-isotope effect on the in-plane penetration depth in the cuprate superconductor $La_{2-x}Sr_xCuO_4$. The observed isotope effect indicates that polaronic charge carriers exist and condense into supercarriers in this cuprate superconductor (see Sec. 10.5.2).

There have been numerous reports in the literature about possible unconventional thermodynamic phases of the vortex matter in ceramic and non-oxide superconductors. The small number of relevant degrees of freedom in vortex-related systems (due to the small number of vortices) represents an attractive challenge for small-signal calorimetry. We are currently building novel thermal probes, not only with the aim to further increase the existing sensitivity for testing bulk thermal properties of such solids, but also to thermally characterize thin-film samples and surfaces (see Sec. 10.6).

This work was done in collaboration with scientists from ETH Zürich (K. Conder, J. Karpinski, H. Schwer, E.M. Kopnin, R. Molinski, and G.I. Meijer), IBM Rüschlikon Laboratory (C. Rossel, H. Rothuizen, J. Brugger, and P. Vettiger), University of Birmingham (E.M. Forgan, S.H. Lloyd, W.J. Nuttall, and P.G. Kealey), University of St. Andrews (S.L. Lee and C. Ager), Institut Max von Laue-Paul Langevin, Grenoble (R. Cubitt), University of Oxford (S.J. Blundell), RIKEN-RAL (F.L. Pratt), University of Warwick (D. McK. Paul), Oak Ridge National Laboratory (M. Yethiraj), Tohoku University (T. Sasaki), Université Paris-Sud (S.T. Johnson), and University of Zaragoza (M.R. Ibarra and J.M. De Teresa).

10.2 Investigating vortex matter at central facilities

The behaviour of magnetic flux in superconductors is of great scientific and technological interest. Pinning the notoriously flexible vortex lines in highly anisotropic superconductors, such as the cuprate high-T_c's is of fundamental importance to any technical application, as movement of flux lines dissipates energy, which presents an unwanted energy-loss. However, on more scientific grounds, the high anisotropy of the cuprate superconductors makes them very interesting systems in the realm of 'soft condensed matter'. The basic building blocks of this type of 'matter', which consist of magnetic flux, are very well understood, such that only the basic interactions between the constituent are decisive for the structures one observes. Studying prime examples of extremely anisotropic superconductors, such as the high-T_c BSCCO and the organic superconductor ET-Cu, we gain an understanding of the generic behaviour and interactions in these systems. Below we will give a small selection of our current work, the details of which can be found in the references.

Muon spin rotation (μSR) and neutron small angle scattering (SANS) present complementary ways of attacking these questions. Both present a microscopic measurement of the bulk of the material, but whereas the muon is a probe of the local fields, neutrons are susceptible to long range modulations in the field distribution. Therefore the fluctuations in the vortex lattice are readily observed with μSR [1], while its overall structure can be easily resolved by SANS [2].

In our investigation of the vortex behaviour in the extremely anisotropic superconductor BSCCO, this complementarity has helped us to clarify the interplay between the static disordering of flux lines along their length induced by point pinning sites, with the effects of thermal fluctuations. In highly anisotropic superconducors, the flux lines can viewed as being composed of two dimensional (2D) entities called 'pancake' vortices. With increasing field, a three dimensional vortex line will decompose into these pancake vortices. We have already observed this effect in BSCCO [3, 4] and also in the organic superconductor ET-Cu [5]. We have this year also studied the angular dependence of this effect [6], which together with the dependence upon doping gives valuable insight on the nature of the interlayer coupling between these pancake vortices [4, 6]. Therefore, at high fields, the vortex structure in highly anisotropic superconductors is disordered along the field direction, due to pinning of individual pancake vortices by e.g. oxygen vacancies. This leads to the loss of scattered neutron intensity above this crossover field [7], as the field contrast is strongly reduced, whereas μSR observes a change in the shape of the field distribution. In a narrow region of the phase diagram just around this crossover field, these static disordering of flux lines due to pinning and the dynamic disorder due to thermal fluctuations compete in such a way to result in increased ordering of the flux lattice along the field. At fields just above the crossover field, we have now observed the reappearence of Bragg scattering above a certain temperature T^1, corresponding to a depinning of vortices [8]. As the thermal excitations are strong enough to depin the individual pancake vortices from their pinning sites, the remaining interlayer coupling leads to an ordering of the vortex lines along the field. This can be seen in Fig. 10.1, where we show the temperature dependence of the scattered neutron inten-

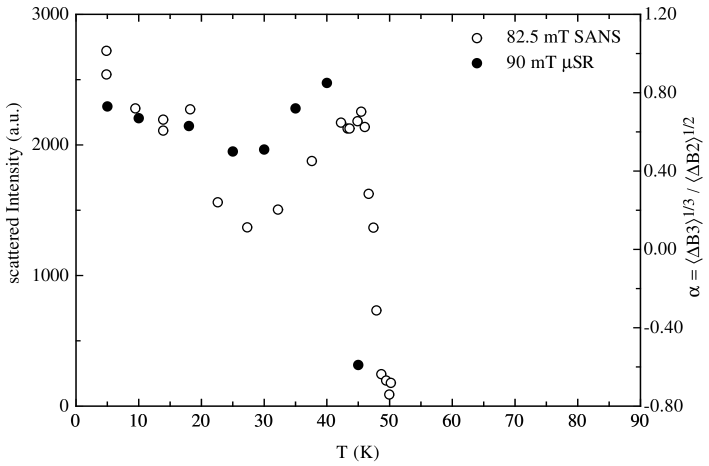

Figure 10.1: *The temperature dependence of the scattered neutron intensity at 82.5 mT showing an upturn at $\sim$ 25 K. This is interpreted as a depinning of pancake vortices (see text). For comparison, the temperature dependence of the lineshape asymmetry α from μSR at 90 mT, is given. The data show an upturn at similar temperatures, indicating increased c-axis correlation in both cases, before the melting transition at higher temperatures.*

sity in a Bragg peak at a field of 82.5 mT. Fig. 10.1 also shows results obtained with μSR, where we have plotted the temperature dependence of the lineshape asymmetry parameter $\alpha = \langle \Delta B^3 \rangle^{1/3} / \langle \Delta B^2 \rangle^{1/2}$. This parameter is positve for lineshapes with a tail extending to fields higher than the average. For a well ordered flux lattice of straight vortex lines, this is expected to be $\sim$ 1.2 in our experimental setup. It can be seen that the lineshape becomes more asymmetric, corresponding to an ordered lattice, at the same point where we observe increased Bragg-scattering. At higher temperatures, the diffraction pattern disappears again, because of the melting of the vortex lattice. We are thus also able to observe the melting of the vortex lattice above the crossover field, which is in contradiction to recent magnetisation experiments [10], where a jump in the reversible magnetisation is interpreted as the melting of the lattice.

We also used the complementarity of neutrons and muons in a study of the differences between type-I and type-II superconductors. With a suitable sample geometry, a type-I superconductor enters the intermediate state, where superconducting regions in the Meissner state coexist with normal-conducting regions with an internal field corresponding to the thermodynamical critical field. This is due to demagnetising effects leading to fields higher than the applied at the sample edges. This effect can be easily seen with μSR, where the local fields are measured. However, the structure of the coexisting domains is unaccesible to the muons, as they only measure locally. SANS in contrast is insensitve to the field values in the normal regions, however the domain structures produce a field contrast, which gives rise to scattering. Thus we can map out the temperature dependence of B_c from μSR, as well as that of the radius of gyration of the domain structures from SANS. By suitably choosing the doping level in PbBi alloys, the Ginzburg-Landau parameter κ, decisive for the overall behaviour, takes on a value for a transition between type-I and type-II superconducing behaviour to be observable. Using the complementarities of SANS and μSR, it is also possible to gain a

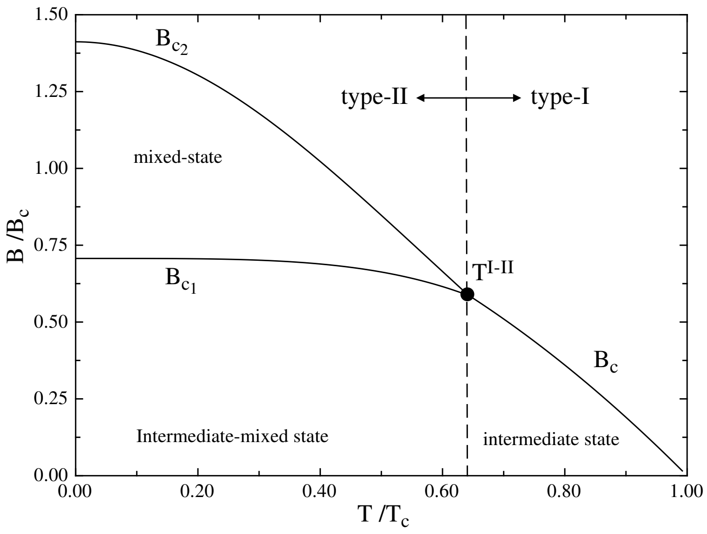

Figure 10.2: *The thermodynamic phase diagram of a superconductor with* κ_0 *=1. The different transition lines corresponding to type-I and type-II superconducting behaviour meet in a multicritical point at a temperature* T^{I-II}*, where the order of the transition changes from first to second order. The phase lines are calculated from the two-fluid model.*

full understanding of the magnetic field structures in the sample. We have even observed a coexistence of type-I and type-II superconducting behaviour for the first time, as could be expected for such a multicritical point in the B-T phase diagram. The thermodynamic phase diagram in accord with these investigations [11] can be calculated from the two-fluid model of superconductivity and is shown in Fig. 10.2.

10.3 Torque magnetization measurements on high-T_c superconductors

10.3.1 Design of a new generation of capacitance sensors for torque magnetometry

The principle of torque magnetometry is to measure magnetic moments of anisotropic magnetic or superconducting samples. The design of a sensor is optimized to detect with a high sensitivity the torque given by $\vec{\tau} = \vec{m} \times \vec{B}$, where $\vec{m}$ is the magnetic moment of the sample and $\vec{B}$ is the homogeneous external magnetic field.
We already developed ultra-sensitive torquemeters based on microscopic silicon cantilevers with piezoresistive readout and a resolution of about 10^{-14} Nm, depending on the operating mode [12] (see also Annual Report 96/97). This sensitivity is sufficient for most applications. The dimensions of these sensors are in the micrometer range in order to better avoid the effects of external mechanical perturbations and to reach a higher sensitivity. These sensors are very well suited for measuring the magnetic moment of very small samples ($< 100\mu$m). However, for larger samples other measurement techniques are required, such as capacitance levers [13, 14] or macroscopic piezoresistive levers [15]. The sensitivity of these devices is always limited by the external mechanical noise and/or by a non-negligible magnetic background of the lever itself.

In collaboration with IBM Rüschlikon we designed a novel silicon torque sensor with capacitive readout and optimal geometry [16]. The advantage of single-crystal silicon, compared to other materials, is its very low magnetic background. The capacitive readout is perfectly suited for high field applications. Furthermore, in order to reach a high mechanical stability,

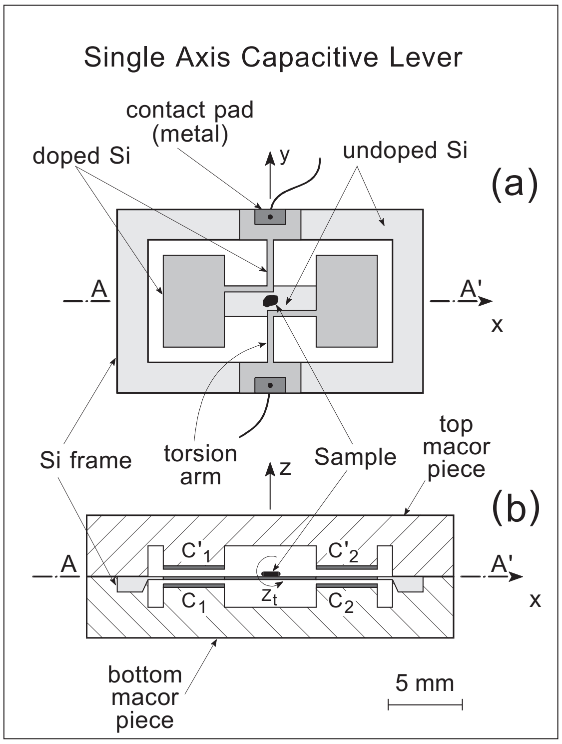

Figure 10.3: *(a) Schematic top view of the torsion lever with its frame. (b) Side view of the lever mounted in the ceramic (macor) support.*

the sensor geometry was chosen to be totally symmetric (see Fig. 10.3a). The flexible torsion lever with its silicon frame is mounted into a ceramic (macor) support which contains two pairs of counterelectrodes. A thin gold layer is patterned on the ceramic surface for the electrical contacts. The torsion lever provides the central electrode, which is positionned in the space between the two pairs of counterelectrodes, forming the capacities C_1, C_1', C_2 and C_2' (see Fig. 10.3b). Any change in position of the lever produces a capacitance variation measured always in a differential mode. Different configurations of electrodes can be chosen, depending on the application. With a specific electronic capacitance bridge, developed by our group, a torque resolution of about $6 \cdot 10^{-13}$ Nm can be achieved.
This novel torquemeter is a powerful tool, not only for further investigations of high-T_c superconductors, but also to study other systems, such as antiferromagnetic compounds [17]. By means of a permanent calibrated magnetic moment (for instance a small piece of Fe_2O_3 audio tape) we were able to calibrate the torquemeter very accurately. On the other hand, with a strong permanent magnet, i.e. NdFeB, the sensor acts as a very sensitive gaussmeter with a typical resolution better than 10 nT.

10.3.2 Doping dependence of superconducting properties in $HgBa_2CuO_{4+\delta}$ single crystals.

High-T_c superconductors show a strong doping dependence of their superconducting properties. Upon increasing the charge carrier concentration, starting from the insulating or semiconducting mother compounds, the critical temperatur T_c increases in the underdoped regime, reaches a maximum for optimal doping and decreases again in the overdoped regime. In the underdoped regime, T_c was found to show a parabolic dependence on the inverse square of the in-plane penetration depth $\lambda_{ab}^{-2}(0) \propto n_s/m_{ab}^*$, where n_s is the density and m_{ab}^* the effective in-plane mass of the superconducting charge carriers [18]. A monotonic increase of the effective mass anisotropy $\gamma = \sqrt{m_c^*/m_{ab}^*}$ with decreasing doping was observed in different experiments using torque magnetometry and other techniques in $YBa_2Cu_3O_{7-\delta}$ [19] and $La_{2-x}Sr_xCuO_4$ [20]. In order to clarify these universal trends, we performed torque measurements on $HgBa_2CuO_{4+\delta}$ single crystals with different oxygen doping δ.

The single crystals were grown using a high pressure growth technique [21]. They were annealed in an Ar or an O_2 atmosphere in order to change δ. We were able to vary δ between 0.05 and 0.11. The superconducting transitions were rather sharp giving evidence for a quite homogeneous oxygen distribution within the samples.

In the layered high-T_c compounds the magnetic moment $\vec{m}$ points preferentally along the c-axis and experiences a magnetic torque $\vec{\tau} = \vec{m} \times \vec{B}_a$ in an applied magnetic field $\vec{B}_a$. In a rotation measurement this magnetic torque is recorded as a function of the angle θ between $\vec{B}_a$ and the ab-plane of the sample. Field dependent measurements at a fixed angle can be performed as well. From the Meissner slope observed at low fields the torque meter can be calibrated.

The $HgBa_2CuO_{4+\delta}$ micro crystals (masses between 1 and 9 μg) were mounted on a small piezoresistive cantilever [22]. Rotation measurements were performed at different temperatures in an applied field $B_a = 1.4$ T. They were analysed using a 3D anisotropic London model [23], revealing the effective mass anisotropy γ, the in-plane penetration depth λ_{ab}, and the upper critical field along the c-axis B_{c2}^c at a given temperature. From the temperature dependence of λ_{ab} and B_{c2}^c their low temperature values were extrapolated. Fig. 10.4a

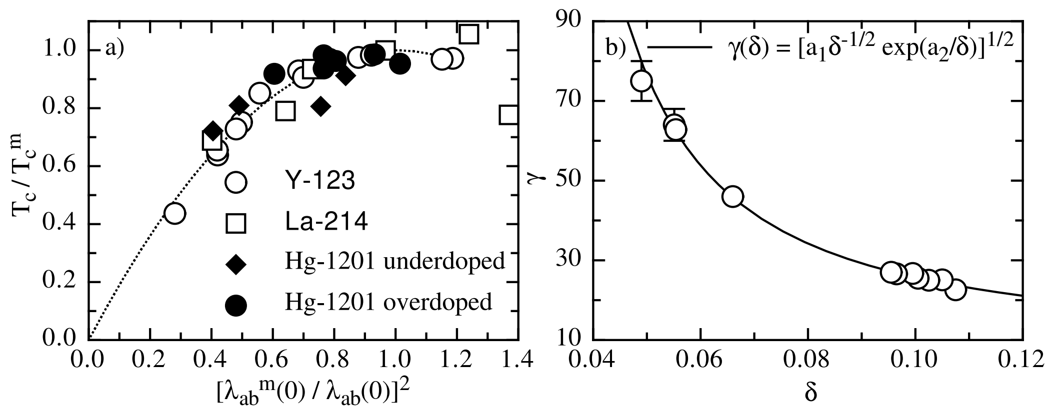

Figure 10.4: *a)* $\overline{T_c}$ *as a function of* $1/\overline{\lambda}_{ab}^2$ *for our samples together with earlier reported data (from Ref. [18]). The dotted line represents the parabolic ansatz* $\overline{T}_c = 2/\overline{\lambda}_{ab}^2(1 - 1/(2\overline{\lambda}_{ab}^2))$. *b) Effective mass anisotropy as a function of doping* δ. *The solid line is based on a (bi)polaronic model of high-*T_c *superconductivity (see text).*

shows the reduced critical temperature $\overline{T}_c = T_c/T_c^m$ as a function of the inverse square of the reduced penetration depth $\overline{\lambda}_{ab} = \lambda_{ab}(0)/\lambda_{ab}^m(0)$ (T_c^m and $\lambda_{ab}^m(0)$ are the values at optimal doping) together with earlier reported data from [18] (Uemura plot). The data in the underdoped regime are well described by the parabolic ansatz $\overline{T}_c = 2/\overline{\lambda}_{ab}^2(1 - 1/(2\overline{\lambda}_{ab}^2))$ [18]. The data for our overdoped samples seem to fall on the same branch, pointing towards an increase of $\lambda_{ab}(0)$ in the overdoped regime with increasing doping. This increase cannot be an artifact due to an overestimation of the superconducting volume, since our calibration of $\lambda_{ab}(0)$ does not depend on the sample volume.

As shown in Fig. 10.4b, γ is monotonically increasing with decreasing δ over the whole doping regime investigated. An explanation for this increase can be given by a (bi)polaronic model of superconductivity by Alexandrov and Mott [24] ,which is supported by experimental evidence for polaronic superconducting carriers in the $La_{2-x}Sr_xCuO_4$ system [25]. Within this model γ mainly depends on the (bi)polaronic binding energy which is predicted by theory to be proportional to $1/\delta$ [26]. With this the effective mass anisotropy is given by $\gamma(\delta) = [a_1\delta^{-1/2}\exp(a_2/\delta)]^{1/2}$. This doping dependence is shown as a solid line in Fig. 10.4b. Since high-quality $HgBa_2CuO_{4+\delta}$ single crystals are very small, there is hardly any other experimental technique to investigate them. Therefore several physical parameters entering in a_1 and a_2 are unknown for the $HgBa_2CuO_{4+\delta}$ system. However, the two values a_1 and a_2 obtained from the fit are in a reasonable range.

The increase of the (bi)polaronic binding energy with decreasing doping also leads to an increase of the effective mass of the normal state charge carriers. This might by an explanation for the observed smooth crossover from metallic to insulating or semiconducting behavior upon reducing the charge carrier concentration [27]. Furthermore this (bi)polaronic model also provides a simple explanation for the linear dependence of γ on the number n of CuO_2 layers in the $HgBa_2Ca_{n-1}Cu_nO_{2n+2+\delta}$ family [28].

10.4 EPR study of cuprates

10.4.1 EPR study of low-dimensional cuprates

Although the study of one-dimensional (1D) magnetism has a very long history, the recent discovery of various quasi-1D quantum antiferromagnets and the progress in analytic and numerical theories have significantly advanced this field [29].

Recently, the novel 1D cuprate $Sr_{0.73}CuO_2$ was synthesized under high oxygen pressure at ETH Zürich [30]. This compound is made of edge sharing CuO chains and the average valency of copper is +2.56. Thus, $Sr_{0.73}CuO_2$ provides an unique possibility to study the properties of hole doped copper-oxygen chains. Perhaps the most peculiar feature of $Sr_{0.72}CuO_2$ is a sudden jump in the magnetization observed below ~10 K, indicating a ferromagnetic-like magnetic transition [30]. We performed EPR measurements in order to study the magnetic properties of $Sr_{0.73}CuO_2$ on a microscopic level [31].

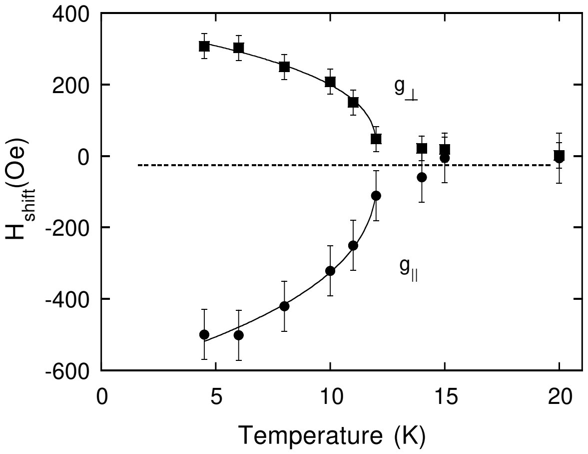

Figure 10.5: *Temperature dependencies of the position of the extra peaks relative to the $g_{||}$ and $g_\perp$ components. The solid lines correspond to a power-law fit (1-T/T_c)$^\beta$ with T_c=12.05(5) K and β=0.34(5).*

The most important results can be summarized as follows. In the paramagnetic regime the EPR signal corresponds to powder averaged spectra with $g_{||}$=2.21(1) and $g_{\perp}$=2.015(5), which is characteristic for Cu^{2+} ions in an axial crystal electric field. Below ~12 K, two new lines split from the main EPR line. With decreasing temperature one line splits from the $g_{||}$ peak and shifts to lower fields, while another line splits from the $g_{\perp}$ peak and shifts to higher fields. The splitting of the EPR line demonstrates that below Tc a well defined internal field develops in $Sr_{0.73}CuO_2$ due to 3D long-range magnetic order. The temperature dependence of the EPR line splitting, which represents a measure of the internal magnetic field present in the sample, is shown in Fig. 10.5. The solid line corresponds to a power-law fit $(1\text{-}T/T_c)^{\beta}$ with T_c=12.05(5) K and β=0.34(5). Our preliminary zero-field μSR measurements on the same sample also confirmed a sharp magnetic transition below Tc [32].

Thus magnetization, EPR, and μSR measurements provide evidence that below T_c ~12 K a long-range magnetic order with a small spontaneous ferromagnetic moment $M_s = 3.2(2) \cdot 10^{-3} \mu_B$/Cu occurs in $Sr_{0.73}CuO_2$ [31]. The observation of magnetic order is very unusual in view of the high hole doping of the copper-oxygen chains, where each hole renders a CuO unit to become nonmagnetic due to the Zhang-Rice singlet formation. Further experimental work is necessary to clarify the microscopic mechanism of this unusual magnetic transition.

10.4.2 EPR study of high-T_c cuprates

There is increasing evidence that inhomogeneous distribution of charge carriers is a common, if not universal, feature of cuprates and that ordering of charge into modulated structures may play a key role in high-temperature superconductivity [33]. However, neither the exact nature of these inhomogeneities nor their influence on the electronic properties are well understood. EPR of magnetic rare earth ions in high-T_c cuprates is a highly sensitive local method, which allows to study spatial variation of structural and electronic properties on a microscopic level [34]. We performed EPR measurements of Yb^{3+} doped to $YBa_2Cu_4O_8$ (Y124) with 1% of the Y replaced by Yb^{3+}. Structurally, Y124 is unique in the sense that it has fixed oxygen stoichiometry with saturated double CuO chains, providing a test case free of ambiguities due to oxygen disorder and nonstoichiometry.

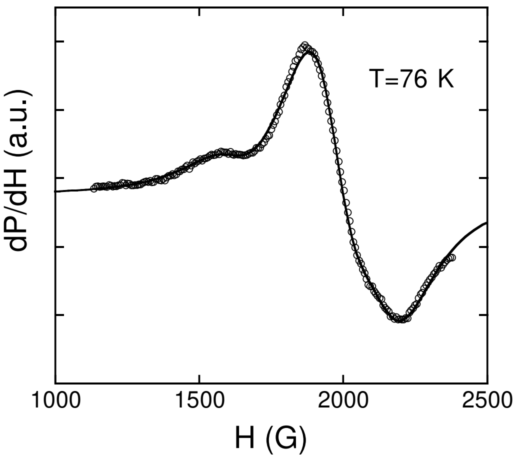

Figure 10.6: *Yb^{3+} EPR spectra of $Y_{0.99}Yb_{0.01}Ba_2Cu_4O_8$ at 76 K. The solid line is a fit using the sum of three Lorentzians with different g-factors.*

Fig. 10.6 shows EPR spectra of Yb^{3+} at 76 K. From Fig. 10.6 one can see that the Yb^{3+} spectra have an asymmetric lineshape with shoulders at the low and high field side of the central line. We found that the spectra can be well described by a sum of three Lorentzian lines of the same linewidth, but with different g-factors. This very likely indicates three different surroundings of Yb^{3+} in Y124 due to crystal electric field variation. It is worth noting that inelastic neutron scattering measurements in $ErBa_2Cu_3O_x$ samples also revealed three different types of clusters in the CuO_2 planes [35]. We plan to extend our measurements to higher frequencies and on magnetically oriented samples in order to clarify this interesting question in more detail.

10.5 Studies of oxygen isotope effects

10.5.1 Oxygen isotope effects in the manganites

The manganese-based perovskites $La_{1-x}Me_xMnO_3$ (Me = Ca, Sr, and Ba) have recently been the subject of intensive investigations because of the discovery of the colossal magnetoresistance (CMR) effect. The manganites exhibit a broad range of electronic and magnetic phases, ranging from low-resistivity ferromagnetic metals to high-resistivity insulators, which are extremely sensitive to variation of composition, temperature and pressure. Such sensitivity also extends to the oxygen isotope exchange: replacing ^{16}O with ^{18}O in $La_{0.8}Ca_{0.2}MnO_{3+y}$ [36], produces an unusually large change in the magnetic properties (a 21 K decrease in the Curie temperature). There are also large oxygen isotope effects on other physical properties such as the thermal-expansion coefficient jump at T_C [37] and the EPR intensity [38]. These isotope-effect experiments provide crucial evidence for the existence of small polarons (JT polarons [39]) in these JT perovskites, and place important constraints on the microscopic mechanism of the colossal magnetoresistance effect.

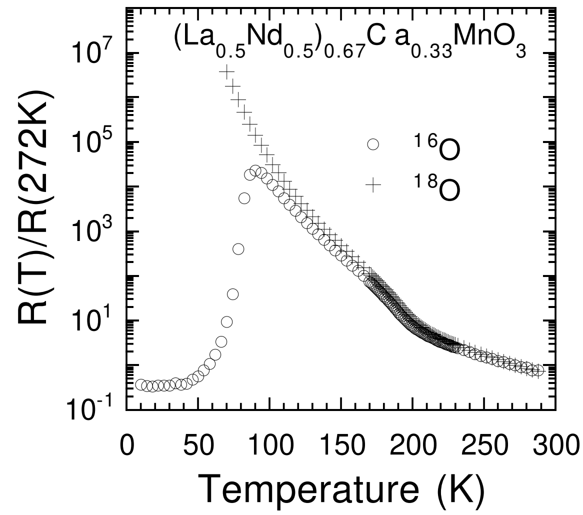

Figure 10.7: *The temperature dependence of the resistivity (normalized to the resistivity at 272 K) for the ^{16}O and ^{18}O samples of $(La_{0.5}Nd_{0.5})_{0.67}Ca_{0.33}MnO_3$.*

We have extended our studies of the oxygen-isotope effects in some chosen manganites such as $(La_{0.5}Nd_{0.5})_{0.67}Ca_{0.33}MnO_3$. This material has a smaller ionic radius at A-site $\langle r_A \rangle$ and much lower T_C than $La_{0.67}Ca_{0.33}MnO_3$. This compound undergoes an insulator-metal transition as it is cooled below $\sim$ 100 K. But it is very surprising that after substituting ^{18}O for ^{16}O, the compound remains in an insulating state down to 5 K (see Fig. 10.7). Note that at low temperatures the resistivity for the ^{18}O samples is too high to measure. This novel isotope effect has never been expected by any conventional theory in condensed matter physics. By considering the presence of both lattice and magnetic polarons in this material, we might be able to explain this experimental result [40]. Recently, this novel insulator-metal transition induced by oxygen isotope exchange was confirmed by a Russian group [41].

To understand the origin of this novel isotope effect, we have also done neutron scattering, magnetostriction and thermal-expansion experiments on this material with both ^{16}O and ^{18}O isotopes. We show that the ^{18}O sample exhibits an antiferromagnetic, charge ordered, and insulating ground state, while the ^{16}O sample has a phase separation: a ferromagnetic state in some regimes and an antiferromagnetic state in other regimes. Upon replacing ^{16}O with ^{18}O, the ferromagnetic regimes transform into the antiferromagnetic regimes. All these results consistently suggest that charge carriers in manganites are strongly coupled to the local JT distortions and magnetic moments, so that small polarons (quasiparticles dressed by both the local JT distortions and spin polarizations) can be formed. This is crucial for the understanding of the physics in the colossal magnetoresistive manganites.

10.5.2 Oxygen isotope effect in $La_{2-x}Sr_xCuO_4$

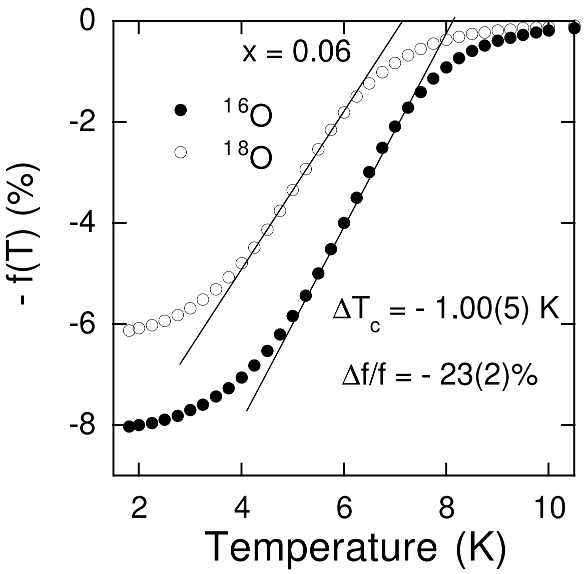

Figure 10.8: *Temperature dependence of the Meissner effect for ^{16}O and ^{18}O samples of $La_{2-x}Sr_xCuO_4$ with $x = 0.06$.*

The microscopic pairing mechanism for high-T_c superconductivity (HTSC) is one of the most controversial issues in condensed matter physics. Eleven years after the discovery of the high-T_c cuprate superconductors by Bednorz and Müller [42], there have been no microscopic theories that can describe the physics of high-T_c superconductors completely and unambiguously. The high values of T_c (>30 K) in the cuprate superconductors were not expected from a conventional phonon-mediated pairing mechanism, so many non-phonon mediated mechanisms have been proposed. A great number of experimental results appear to support some of these unconventional mechanisms. On the other hand, there is increasing experimental evidence that a strong electron-phonon coupling is present in cuprates. Such strong electron-phonon interaction may lead to the formation of polaronic charge carriers. Still, direct evidence that polarons exist in the copper oxides has been lacking, although some indirect evidence comes from their recent discovery [36] in the structurally similar but nonsuperconducting manganite $La_{1-x}Ca_xMnO_3$.

To show that polaronic charge carriers exist and condense into supercarriers, one has to

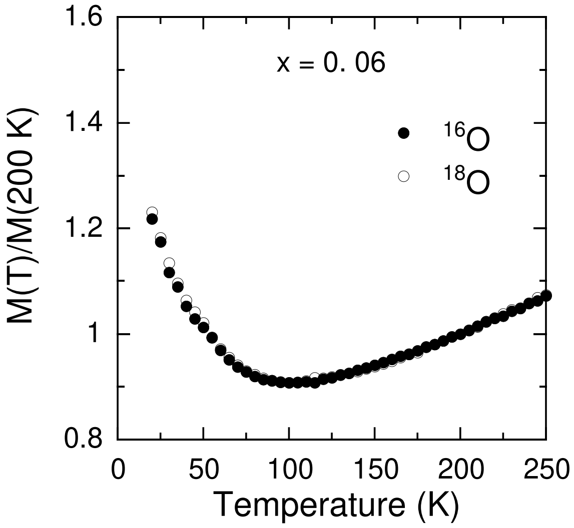

Figure 10.9: *Normal-state susceptibility for ^{16}O and ^{18}O samples of $x = 0.06$. From the doping dependence of the normat-state susceptibility, we estimate that the difference in the hole concentrations of the two isotope samples must be less than 0.0002 per cell.*

demonstrate that the effective supercarrier mass depends strongly on the ionic mass M. This is because the effective mass of polarons depends strongly on M (Ref. [24]). When the polarons condense into supercarriers by whatever pairing mechanism, the effective supercarrier mass will also depend on M. We have performed magnetization measurement on samples of the one-layer cuprates $La_{2-x}Sr_xCuO_4$ as a function of x $(0.06 \leq x \leq 0.15)$. From magnetization measurements on the fine-grained and decoupled samples in the Meissner state, we find substantial oxygen-isotope effects on both the penetration depth $\lambda(0)$ and T_c (see Fig. 10.8) [25]. From normal-state susceptibility measurements, we are able to show that there is a negligible oxygen-isotope effect on the carrier density n (see Fig. 10.9). The combined results strongly suggest that there is an oxygen-isotope effect on the effective supercarrier mass m^{**}, which is huge for $x = 0.06$, and reduced to a smaller value for $x = 0.15$. From the normal-state susceptibility, we have also determined the normal-state gap as a function of x on the basis of small (bi)polaron theory [26]. We discuss the isotope effects, supercarrier mass anisotropy, normal-state gap, in-plane penetration depth and mid-IR spectra for $x \leq 0.09$ on the basis of the small polaron theory of superconductivity. We find that the agreement between the calculated and experimental results is excellent without any adjustable parameters.

10.6 Detection of small thermal effects in basic and applied condensed matter physics

An important source of progress in experimental condensed-matter physics is the development of new measuring techniques with very high accuracy. The application of high-precision techniques already allowed for the observation of very small thermodynamic effects such as phase transitions of the vortex matter in cuprate superconductors[43, 44, 45], that finally led to exciting new insights into the fundamentals of material properties limiting current transport. These innovative experimental methods shall be extended at our institute, not only with the aim to further increase the sensitivity for testing bulk thermal properties of solids, but also to develop novel tools to thermally characterise thin-film samples, surfaces, and small artificial structures.

We intend to study the possibility of measuring thermal effects locally, e.g. on single crystals or thin films. There are already several apparatuses described in the literature that produce rough thermal images of solid-state surfaces at or above room temperature [46]. A logical improvement is to detect locally small changes in temperature as a function of time (the knowledge of which is necessary to calculate a specific heat), and to finally place such an experiment into a cryostat. Natural applications of such a device are the (notably non-destructive) imaging of thermal properties of materials showing domains or a coexistence of thermodynamic phases, the measurement of the thermal conductivity on thin-film samples (e.g., thermoelectric materials), and the thermal imaging of artificial structures like microelectronic control elements, sensors, and circuits under operation, at or below room temperature.

References

[1] S.L. Lee *et al.*, Phys. Rev. Lett. **75**, 922 (1995).

[2] D.McK. Paul *et al.*, Phys. Rev. Lett. **80**, 1517 (1998).

[3] S.L. Lee *et al.*, Phys. Rev. Lett. **71**, 3862 (1993).

[4] C.M. Aegerter *et al.*, Phys. Rev. B **54**, R15661 (1996).

[5] S.L. Lee *et al.*, Phys. Rev. Lett. **79**, 1563 (1997).

[6] C.M. Aegerter *et al.*, Phys. Rev. B **57**, 1253 (1998).

[7] R. Cubitt *et al.*, Nature **365**, 407 (1993).

[8] S.H. Lloyd *et al.*, submitted to Phys. Rev. Lett. (1998).

[9] S.L. Lee *et al.* Phys. Rev. B **55**, 5666 (1997).

[10] B. Khaykovich *et al.* Phys. Rev. Lett. **76**, 2555 (1996).

[11] C.M. Aegerter *et al.*, submitted to Phys. Rev. B (1998).

[12] M. Willemin *et al.*, J. Appl. Phys. **83**, 1163 (1998).

[13] R. Griessen *et al.*, Phys. Rev. B **16**, 4385 (1977).

[14] H. Schnack, PhD Thesis, *Vrije Universiteit*, Amsterdam, (1995).

[15] Physics Today **51**, 14 (1998).

[16] C. Rossel and M. Willemin, IBM Technical Disclosure Bulletin **40**, 119 (1997).

[17] G.I. Meijer *et al.*, to appear in Europhys. Lett. (1998).

[18] T. Schneider and H. Keller, Phys. Rev. Lett. **69**, 3374 (1993); Int. J. Mod. Phys. **8**, 487 (1993).

[19] T. R. Chien *et al.*, Physica C **229**, 273 (1994).

[20] M. Suzuki and M. Hikita, Phys. Rev. B **44**, 249 (1991).

[21] J. Karpinski *et al.*, Physica C **234**, 10 (1994).

[22] C. Rossel *et al.*, J. Appl. Phys. **79**, 8166 (1996).

[23] V.G. Kogan, M.M. Fang, and S. Mitra, Phys. Rev. B **38**, 11958 (1988).

[24] A.S. Alexandrov and N.F. Mott, Int. J. Mod. Phys. **8**, 2075 (1994).

[25] G.M. Zhao *et al.*, Nature **385**, 236 (1997).

[26] A.S. Alexandrov, V.V. Kabanov, and N.F. Mott, Phys. Rev. Lett. **77**, 4796 (1996).

[27] H. Takagi *et al.*, Phys. Rev. B **40**, 2254 (1989).

[28] J. Hofer, unpublished results.

[29] E. Dagotto and T.M. Rice, Science **271**, 618 (1996).

[30] J. Karpinski *et al.*, Physica C **274**, 99 (1997).

[31] A. Shengelaya *et al.*, Phys. Rev. Lett. (1998) in press.

[32] A. Shengelaya *et al.*, (unpublished).

[33] See, for instance, *Phase separation in Cuprate Superconductors*, edited by K.A. Müller and G. Benedek (World Scientific, Singapore, 1993).

[34] A. Jánossy *et al.*, Physica C **171**, 457 (1990).

[35] J. Mesot *et al.*, Phys. Rev. Lett. **70**, 865 (1993).

[36] G.M. Zhao *et al.*, Nature **381**, 676 (1996).

[37] G.M. Zhao, M.B. Hunt and H. Keller, Phys. Rev. Lett. **78**, 955 (1997).

[38] A. Shengelaya *et al.*, Phys. Rev. Lett. **77**, 5296 (1996).

[39] K.-H, Höck, H. Nickisch, and H. Thomas, Helv. Phys. Acta. **56**, 237 (1983).

[40] G.M. Zhao *et al.*, Solid State Commun. **104**, 57 (1997).

[41] N.A. Babushkina *et al.*, Nature **391**, 159 (1998).

[42] J.G. Bednorz and K.A. Müller, Z. Phys. B **64**, 189 (1986)

[43] A. Schilling and O. Jeandupeux, Phys. Rev. B **52**, 9714 (1995).

[44] A. Schilling *et al.*, Nature **382**, 791 (1996).

[45] A. Schilling *et al.*, Phys. Rev. Lett. **78**, 4833 (1997).

[46] J. Kölzer *et al.*, Microelectronic Engineering **31**, 251 (1996).